



PCCP

**Investigation of mechanical properties and structural integrity of graphene aerogels via molecular dynamics simulations**

Journal:	<i>Physical Chemistry Chemical Physics</i>
Manuscript ID	CP-ART-06-2023-002585.R1
Article Type:	Paper
Date Submitted by the Author:	17-Jul-2023
Complete List of Authors:	Zheng, Bowen; University of California Berkeley, Mechanical Engineering Liu, Chen; Stanford University Li, Zhou; Stanford University, Carraro, Carlo; University of California Berkeley, Chemical and Biomolecular engineering Maboudian, Roya; University of California Berkeley Senesky, Debbie; Stanford University, Aeronautics & Astronautics Gu, Grace; University of California Berkeley, Mechanical Engineering

SCHOLARONE™  
Manuscripts

## Investigation of mechanical properties and structural integrity of graphene aerogels via molecular dynamics simulations

Bowen Zheng<sup>1</sup>, Chen Liu<sup>2</sup>, Zhou Li<sup>3,4</sup>, Carlo Carraro<sup>4</sup>, Roya Maboudian<sup>4</sup>, Debbie G. Senesky<sup>3,5</sup>, and Grace X. Gu<sup>1,\*</sup>

<sup>1</sup>Department of Mechanical Engineering, University of California, Berkeley, CA 94720, United States

<sup>2</sup>Department of Mechanical Engineering, Stanford University, CA 94305, United States

<sup>3</sup>Department of Aeronautics & Astronautics, Stanford University, CA 94305, United States

<sup>4</sup>Department of Chemical and Biomolecular Engineering, and Berkeley Sensor & Actuator Center, University of California, Berkeley, CA 94720, United States

<sup>5</sup>Department of Electrical Engineering, Stanford University, CA 94305, United States

### Abstract

Graphene aerogel (GA), a 3D carbon-based nanostructure built upon 2D graphene sheets, is well known for being the lightest solid material ever synthesized. It also possesses many other exceptional properties such as high specific surface area and large liquid absorption capacity thanks to its ultra-high porosity. Computationally, the mechanical properties of GA have been studied by molecular dynamics (MD) simulations, which uncover nanoscale mechanisms beyond experimental observations. However, studies on how GA structures and properties evolve in response to simulation parameter changes, which provide valuable insights to experimentalists, have been lacking. In addition, the differences between calculated properties via simulations and experimental measurements have rarely been discussed. To address the shortcomings above, in this study, we systematically study various mechanical properties and the structural integrity of GA as a function of a wide range of simulation parameters. Results show that during the *in silico* GA preparation, smaller and less spherical inclusions (mimicking the effect of water clusters in experiments) are conducive to strength and stiffness but may lead to brittleness. Additionally, it is revealed that a structurally valid GA in the MD simulation requires the number of bonds per atom to be at least 1.40, otherwise the GA building blocks are not fully interconnected. Finally, our calculation results are compared with experiments to showcase both the power and the limitations of the simulation technique. This work may shed light on the improvement of computational approaches for GA as well as other novel nanomaterials.

### Introduction

Graphene is a two-dimensional (2D) structure of carbon atoms with extraordinary electronic,<sup>1, 2</sup> thermal,<sup>3-6</sup> and mechanical<sup>7-10</sup> properties. However, when graphene is encapsulated into polymers, the properties of resulting polymeric composites are not as good as theoretical predictions, due to the poor dispersion quality of the 2D graphene materials in the matrix. To fully exploit the high potential of graphene, various 3D structures such as graphene foams,<sup>11-13</sup> graphene aerogels<sup>14-16</sup> and graphene networks<sup>17-20</sup> are explored, which are better at preserving the unique properties of graphene in real use cases. Among these 3D structures, graphene aerogel (GA) stands out, thanks mainly to its ultra-low density and high porosity up to 99%.<sup>14, 21</sup> As the lightest solid material ever synthesized, GA has been proposed as a substitute for rare and expensive helium.<sup>22</sup> As a highly porous material with a large surface area, GA has been explored as a sorbent for environment remediation<sup>23-26</sup> and effective catalytic scaffolds<sup>27-29</sup>. Additionally, GAs show many other useful physical properties such as high conductivity<sup>15, 30</sup> and compressibility<sup>16, 31</sup>. Therefore, GAs have also been considered as a promising material for supercapacitors,<sup>32-34</sup> gas sensing,<sup>35, 36</sup> energy absorption,<sup>16, 37, 38</sup> among many other applications.

Among the various properties of GAs, the mechanical property has been widely researched, since the graphene building block is the strongest material ever tested. Both experimental and computational studies have been conducted on the mechanical property of GA. Experimentally, Zhu et al. fabricated GAs via 3D printing and showed that GAs exhibit supercompressibility and are much stiffer than bulk graphene of comparable density.<sup>31</sup> Cheng et al. showed that a GA cylinder with a density of 56.2 mg·cm<sup>-3</sup> could support at least 26,000 times its own weight and recover to its original state without permanent deformation<sup>39</sup>. Zhang et al. reported that GA–polydimethylsiloxane composites exhibit extremely large deformability in both tension and compression.<sup>40</sup>

Computationally, molecular dynamics (MD) simulations have been favored by researchers due to their capability in shedding light on detailed mechanical responses of nanomaterials that are beyond the experimental capabilities. Qin et al. showed in MD simulations that GA can be 10 times as strong as mild steel at a density of 4.6% that of mild steel, but the mechanical properties decrease with density faster than those of polymer foams<sup>22</sup>. Patil et al. studied the fracture behavior<sup>41</sup> and the shock wave response<sup>42</sup> using MD simulations, and showed that GAs have good shockwave and energy absorption abilities. Zheng et al. quantified the uncertainty of GAs arising from the structure randomness using Gaussian process metamodels.<sup>43</sup>

However, there have been some shortcomings in previous MD simulation works. First, the properties of GAs have not been extensively studied in response to changes in simulation variables. Previous studies have only examined very few parameters (mainly the radius of inclusions) while many other parameters such as the inclusion-to-flake ratio, the total number of particles in the simulation, and the annealing properties can have a great impact on the GA properties. Second, the structural integrity of GAs in MD simulations has not been studied against changes in the variables. Number of bonds per atom has been used as a metric to quantify how well graphene flakes are connected inside a GA structure. However, it has not been investigated how this metric changes in response to changes of simulation parameters. Third, there has been a deviation of an order of magnitude between densities in MD simulations and experiments. GAs with a density below  $10 \text{ mg}\cdot\text{cm}^{-3}$  have been fabricated in experiments, while the lowest density studied in MD simulations is around  $100 \text{ mg}\cdot\text{cm}^{-3}$ . Lastly, to the best of our knowledge, there has not been any reported research that directly compares MD simulation results with experimental data.

In this paper, we aim to address the above challenges as well as to discuss the limitations of MD simulations in modeling GAs. First, various mechanical properties as a function of a broad set of simulation parameters are studied. Second, the structural integrity of GAs is quantified and evaluated as simulation parameters change. Additionally, the reason why the density of GA in MD simulations cannot reach the low values obtained experimentally is discussed. Finally, our findings are compared with experimental results to showcase both the power and the limitations of the simulation technique.

## Results and Discussion

### *Graphene aerogel structure generation in molecular dynamics simulations*

Adopting the approach of previous simulation studies,<sup>22, 41, 43</sup> a GA structure is formed via condensing an initially sparse and disconnected system into an integrated structure. The initial system for the GA preparation is a cubic box consisting of graphene flakes and spherical inclusions, as shown in Fig. 1a. The periodic boundary condition is applied in all three dimensions to approximate an infinitely large system. The inclusions mimic the effect of water clusters in freeze-casting porous graphene materials<sup>44</sup>. The numbers of graphene flakes and inclusions are denoted by  $N_{\text{flake}}$  and  $N_{\text{inc}}$ . The initial density is set as low as  $1 \text{ mg}\cdot\text{cm}^{-3}$  to minimize the probability of overlapping atoms. Graphene flakes are square-shaped with a side length  $L$ , while the inclusions are modeled as spheres with an effective radius  $R_{\text{eff}}$ , as illustrated in Fig. 1b.  $R_{\text{eff}}$  is mathematically defined as  $R_{\text{eff}} = 2^{1/6}\sigma$ , where  $\sigma$  is a parameter of the Lennard-Jones potential that models the equilibrium spacing between two particles (detailed in the Methods section). Because  $R_{\text{eff}}$  and  $\sigma$  are proportional, in this paper, “the effect of  $R_{\text{eff}}$ ” and “the effect of  $\sigma$ ” are used interchangeably. In our study, the values of  $L$  within one simulation system follows various distributions, which has not been studied in previous work. We consider the distribution of  $L$  a variable and aim to study its effect on the mechanical and structural properties of GAs. One distribution that  $L$  follows is the log-normal distribution, of which the probability density function is

$$p(L) = \frac{1}{L\sigma_{\ln}\sqrt{2\pi}} e^{-\frac{1}{2}\left(\frac{\log L - \mu_{\ln}}{\sigma_{\ln}}\right)^2} \quad (1)$$

where

$$\sigma_{\ln} = \sqrt{\log\left(\frac{L_{\text{std}}}{\bar{L}^2} + 1\right)} \quad (2)$$

and

$$\mu_{\ln} = \log \bar{L} - \frac{\sigma_{\ln}^2}{2} \quad (3)$$

In this study,  $\bar{L} = 12 \text{ \AA}$  and  $L_{\text{std}} = 4.8 \text{ \AA}^2$  are used. By default,  $L$  follows the log-normal distribution.  $L$  is also modeled with half normal distributions, of which the probability density function is

$$p(L) = \sqrt{\frac{2}{\pi}} \frac{1}{\sigma_{\text{hn}}} e^{-\frac{1}{2}\left(\frac{L - \mu_{\text{hn}}}{\sigma_{\text{hn}}}\right)^2}, L \leq \mu_{\text{hn}} \quad (4)$$

where  $\mu_{\text{hn}}$  and  $\sigma_{\text{hn}}$  are the location and the scale parameters. In this study,  $\mu_{\text{hn}}$  is set as the largest  $L$  that is sampled by the log-normal distribution to favor larger graphene flakes.  $\sigma_{\text{hn}}$  is a variable that controls the “width” of the half bell curve: larger  $\sigma_{\text{hn}}$  gives wider half bell curve.

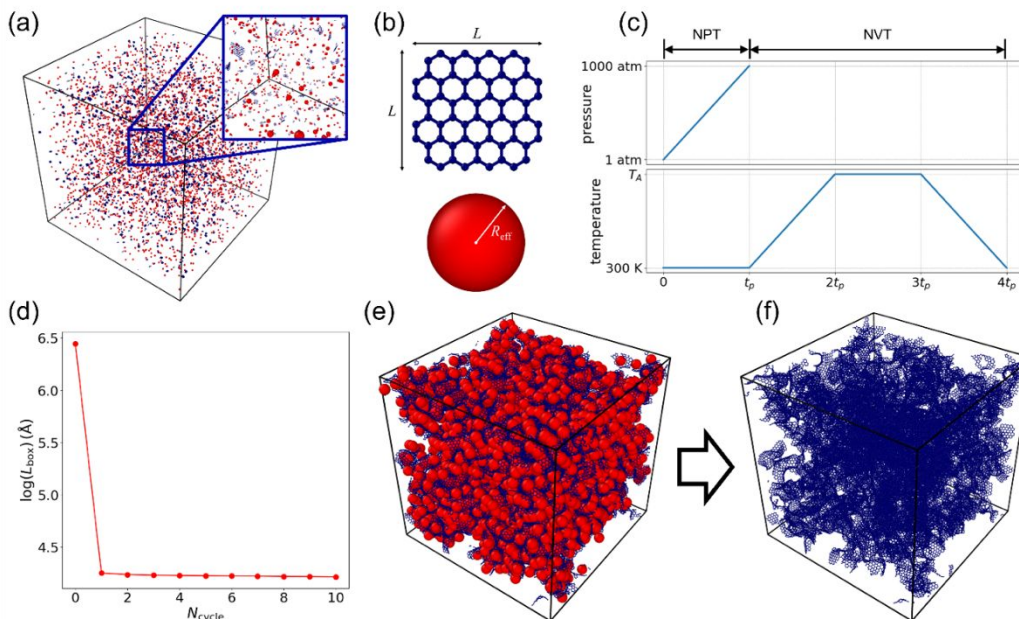


**Figure 1.** Construction of GA structures in the MD simulation. (a) Initial material system where  $N_{\text{flake}} = 500$  and  $N_{\text{inc}} = 1000$ . (b) Dimensions of the graphene flake and the spherical inclusion. (c) Pressure and temperature profiles during one annealing cycle. (d)  $\log(L_{\text{box}})$  as a function of  $N_{\text{cycle}}$ , where  $L_{\text{box}}$  denotes the side length of the cubic simulation box. (e) Condensed material system after 10 annealing cycles. (f) Final GA structure after the removal of inclusions.

Next, a number of designed annealing cycles are applied to condense the material system and to connect graphene flakes into an integrated structure. The total and the current number of annealing cycles is denoted by  $N_{\text{cycles}}$  and  $N_{\text{cycle}}$ , respectively. Each annealing cycle consists of four stages and each has a time duration  $t_p = 50 \text{ ps}$ : (a) in the isothermal–isobaric (NPT) ensemble the pressure increases linearly from 1 atm to 1000 atm and the temperature is maintained at 300 K; (b) in the canonical (NVT) ensemble the temperature increases linearly from 300 K to the annealing temperature  $T_A$ ; (c) in the NVT ensemble the temperature is held at  $T_A$ ; (d) in the NVT ensemble the temperature decreases linearly from  $T_A$  to 300 K. The annealing cycle design is similar to previous MD simulation work<sup>22, 41, 43</sup>. However, in this work, the annealing temperature  $T_A$  is considered a variable. Because the temperature affects the level of movements of graphene flakes, it dictates the probability of graphene flakes encountering each

other and forming bonds, thus affecting the final GA structure. The annealing cycle design described above is illustrated in Fig. 1c.

During the annealing process the system volume decreases sharply in the first cycle and gradually in subsequent cycles, as shown in Fig. 1d. After many annealing cycles, a compact system with interconnected graphene flakes and inclusions can be obtained, as shown in Fig. 1e. Inclusions resemble water clusters in experiments which will be removed from the system during a drying process. Deleting the inclusions and followed by another NVT process for 50 ps, the final stable GA structure in the simulation is obtained, as shown in Fig. 1f. The final relaxation is intended to eliminate the initial stress after annealing cycles. Stress-strain curves with and without the relaxation process are provided in the SI (Figs. S1 and S2), where the latter introduces an initial stress. Full details of MD simulations are provided in the Methods section.

### *Mechanical properties of graphene aerogels*

After the *in silico* fabrication of the GA structure described in the previous section, uniaxial tensile and compressive loads are applied to calculate the mechanical properties of the GA. In this work, loads are applied in a quasi-static, incremental manner. At each step, the simulation box is deformed for a 1% uniaxial strain in the  $x$  direction in the NPT ensemble with a temperature of 300 K and a pressure of 1 atm maintained in the two unloaded  $y$  and  $z$  directions. Each strain increment is followed by an energy minimization and equilibration process in the NVT ensemble at 300 K. Under these loading conditions, a range of mechanical properties of GAs including density  $\rho$ , tensile strength  $\sigma_u$ , tensile failure strain  $\epsilon_u$  (defined as the strain at the maximum tensile stress), tensile and compressive moduli  $E_t$  and  $E_c$  can be computed. We are interested in systematically investigating how these mechanical properties change in response to changes of an extensive set of simulation variables, and we aim to cover more variables than previous studies. In the following, the effects of various simulation variables are studied, including the effective radius of inclusions  $R_{\text{eff}}$  (or  $\sigma$ ), inclusion-to-flake ratio  $R = N_{\text{inc}}/N_{\text{flake}}$ , the total number of particles  $N_{\text{total}} = N_{\text{inc}} + N_{\text{flake}}$ , the annealing temperature  $T_A$ , and the distribution of the side length of graphene flake  $L$ . When a parameter is not studied as a variable, the following values will be used as default:  $N_{\text{flake}} = 200$ ,  $R = 1.0$ ,  $\sigma = 5.0 \text{ \AA}$ ,  $N_{\text{cycles}} = 10$ ,  $T_A = 2000 \text{ K}$ , and  $L$  follows the log-normal distribution described in Eq. 1, unless otherwise specified.

We start by studying the effect of effective radius of inclusions  $R_{\text{eff}}$  (or equivalently,  $\sigma$ ) on the mechanical properties of GAs. Intuitively, larger inclusions result in a higher porosity because these inclusions tend to push the graphene flakes away from each other, as illustrated in Fig. 2a. Here, various mechanical properties of GA as a function of  $\sigma$  are calculated. Each data point on these graphs is based on 5 different random seeds and the error bar represents one standard deviation. Fig. 2b shows that as  $\sigma$  increases, the density  $\rho$  decreases. This is consistent with previous studies<sup>43</sup>. Fig. 2c shows that as  $\sigma$  increases, the tensile strength  $\sigma_u$  decreases. However, this result presents larger error bars compared to the density results. This is because the failure of the GA structure has a stronger dependency on local structural details, and different random seeds give rise to diverse GA structures despite similar densities. The similar applies to the tensile failure strain  $\epsilon_u$ , which also depends strongly on the local structure. However, the trend is opposite to the tensile strength, as shown in Fig. 2d – as  $\sigma$  increases, the failure strain  $\epsilon_u$  increases. This suggests that GAs with a more loosely interconnected microstructure exhibit higher ductility compared with those with a tightly packed microstructure. The moduli under tension and compression are also calculated. Both tensile and compressive moduli  $E_t$  and  $E_c$  decrease as  $\sigma$  increases, and GAs are stiffer under tension than under compression, as shown in Figs. 2e and 2f. The effect of another Lennard-Jones parameter  $\epsilon$ , the depth of the potential well, is also studied. It is shown in the SI (Fig. S3) that the mechanical properties of GAs are not strongly dependent on  $\epsilon$ .

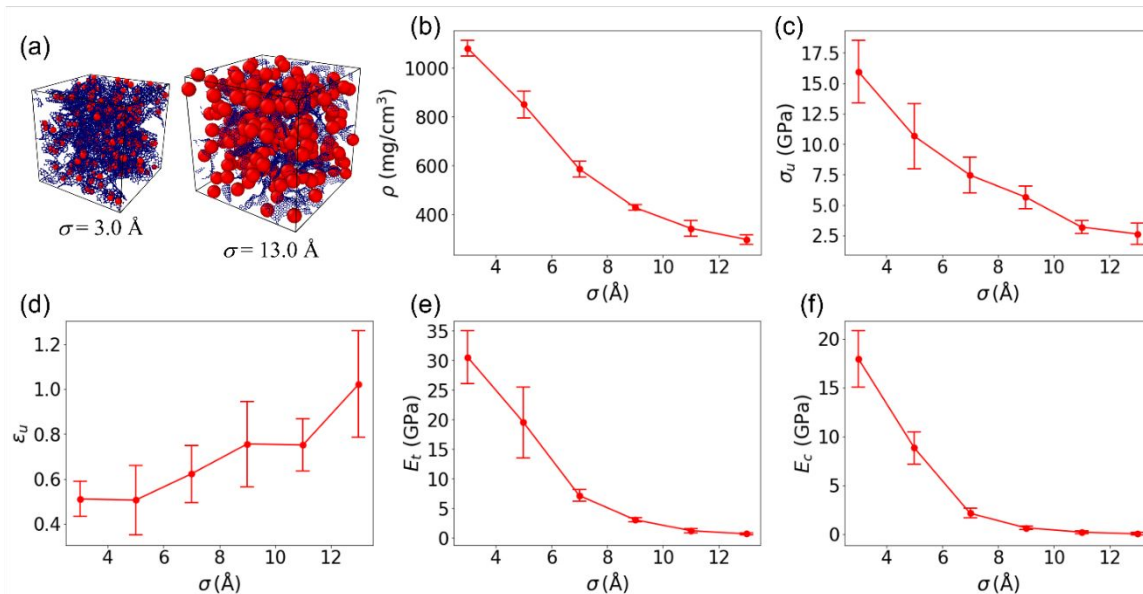


**Figure 2.** Mechanical properties of GA as a function of  $\sigma$ , proportional to the effective radius of inclusions. (a) Illustration of the effect of  $\sigma$ . (b) Density  $\rho$ , (c) tensile strength  $\sigma_u$ , (d) tensile failure strain  $\epsilon_u$ , (e) tensile and (f) compressive moduli  $E_t$  and  $E_c$  of GA as a function of  $\sigma$ .

Next, the effect of the inclusion-to-flake ratio  $R$  is studied, which has not been researched in previous studies. Intuitively, the higher the inclusion-to-graphene ratio, the lower the GA density, since inclusions (which will eventually be removed from the system) occupy larger and larger volume, as illustrated in Fig. 3a. This effect should be similar to the effect radius of inclusion, but via a different mechanism. Results are summarized in Figs. 3b-f, where each data point is based on 5 random seeds. The trends resemble those with  $\sigma$  as the variable, where  $\rho$ ,  $\sigma_u$ ,  $E_t$ ,  $E_c$  decrease and  $\epsilon_u$  increases as  $R$  increases. However, the error bars are larger, indicating that adding more inclusions introduces more uncertainty compared with enlarging  $\sigma$ . The result also hints that to achieve a low-density GA, one can use a large  $\sigma$  together with a high  $R$ . The caveat is that too many inclusions together with a large  $\sigma$  can result in disconnected graphene flakes after the annealing cycles, as shown in the example in the SI (Fig. S4). Additionally, it is shown that increasing the number of annealing cycles does not resolve the issue, as shown in the SI (Fig. S5). A remedy for this issue is to increase the annealing temperature, hoping to increase the possibility of graphene flakes bumping into each other and forming bonds. The temperature effect on the GA structure will be presented in a later section. It is worth noting that fracture-related properties such as  $\sigma_u$  and  $\epsilon_u$  are sensitive to local GA structures, which varies across different random seeds. Consequently, these results bear larger error bars in Figs. 2 and 3. On the contrary, fracture-independent properties such as  $\rho$ ,  $E_t$  and  $E_c$  bear smaller error bars. We have quantified the uncertainty of GA mechanical properties in our previous research using Gaussian process metamodels.<sup>43</sup>

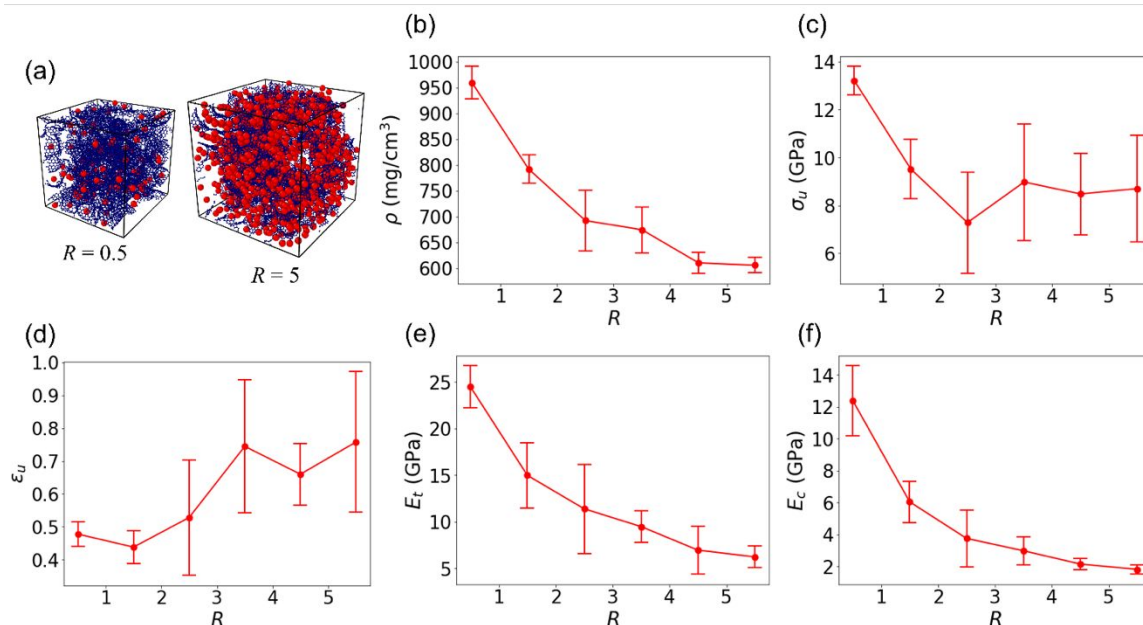


**Figure 3.** Mechanical properties of GA as a function of the inclusion-to-flake ratio  $R$ . (a) Illustration of the effect of  $R$ . (b) Density  $\rho$ , (c) tensile strength  $\sigma_u$ , (d) tensile failure strain  $\epsilon_u$ , (e) tensile and (f) compressive moduli  $E_t$  and  $E_c$  of GA as a function of  $R$ .

Next, the effect of the total number of particles is studied, and the results are summarized in the SI (Fig. S6). The inclusion-to-flake ratio is fixed at  $R = 2.0$  and various  $N_{\text{flake}}$  values are used to achieve material systems of different sizes, as illustrated in Fig. S6a. In our simulations the periodic boundary conditions are applied in all three spatial dimensions, which approximate an infinitely large system by repeating the unit cell. However, it is more realistic and ideal to use a relatively large repeating unit cell to add to the structural diversity and to reduce randomness. The mechanical properties as a function of the total number of particles is less intuitive compared with the previous two variable choices. Again,  $\rho$ ,  $\sigma_u$ ,  $\epsilon_u$ ,  $E_t$ , and  $E_c$  are evaluated as a function of  $N_{\text{flake}}$ . Results are shown in Figs. S5(b-f), where all the mechanical properties of interest decrease as  $N_{\text{flake}}$  increases. In addition, for all properties, the error bars become smaller as the number of particles increases. This suggests that using more particles approaches a homogenized material system which is less sensitive to local randomness. This effect shows especially for the tensile failure strain  $\epsilon_u$  which depends on local structures most. Nevertheless, the computational cost grows exponentially with the increase of number of particles in the simulation.

Of high interest is how the various mechanical properties change as a function of density  $\rho$ , which are properties without variables of simulation artifacts and can relate better to the real material. We plot tensile strength  $\sigma_u$ , tensile failure strain  $\epsilon_u$ , tensile and compressive moduli  $E_t$  and  $E_c$  as a function of density  $\rho$  with all simulation results in this work to observe the general trends, as shown in Fig. 4. The tensile strength and moduli increase as the density increases, which agrees with our intuition, as shown in Figs. 4(a, c, d). On the contrary, as shown in Fig. 4b, the tensile failure strain decreases as the density increases, which agrees with the results in reference<sup>41</sup>.

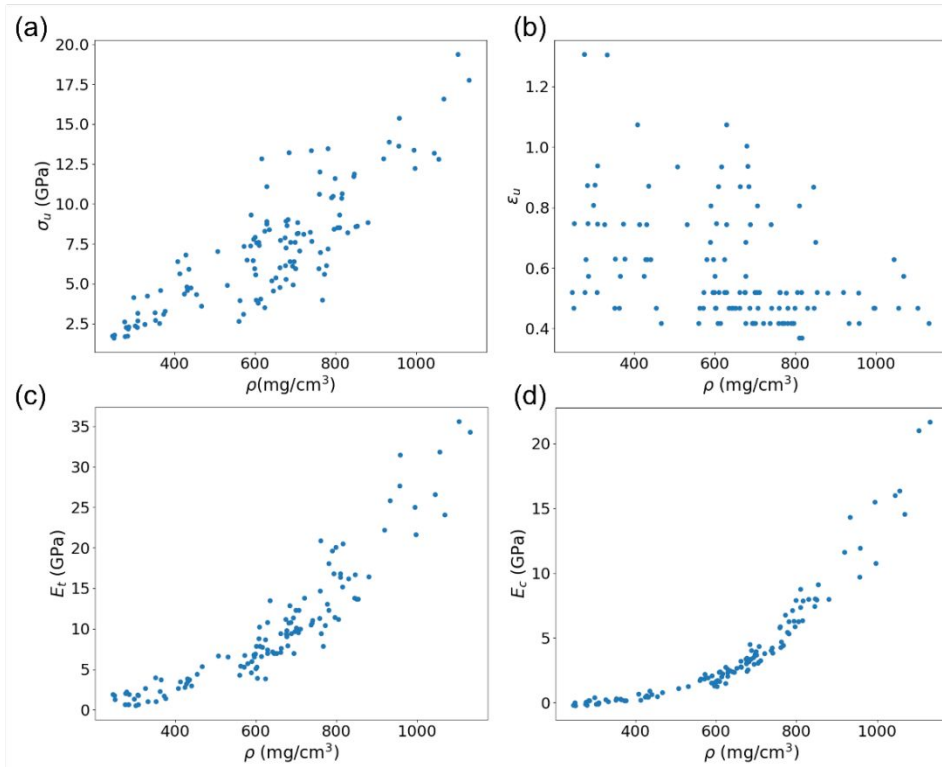


**Figure 4.** Mechanical properties of GA as a function of density  $\rho$  for all well-formed GAs. (a) tensile strength  $\sigma_u$ , (b) tensile failure strain  $\epsilon_u$ , (c) tensile and (d) compressive moduli  $E_t$  and  $E_c$  of GA as a function of  $\rho$ .

#### *Structural integrity of graphene aerogels in molecular dynamics simulations*

The application of annealing cycles does not guarantee that a well-connected GA structure can be formed. In this work, many failed GA structures are observed where graphene flakes are not properly interconnected even after more than 10 annealing cycles, examples shown in the SI (Figs. S3 and S4). This aspect of MD simulations of GAs has not been discussed in the literature, and may explain why the ultra-low density of real GAs has been difficult to be achieved in MD simulations. In this work we aim to shed light on this aspect.

Previous work used the number of bonds per atom  $N_{\text{bond/atom}}$  to quantify the connectivity of graphene flakes. For an infinitely large planar graphene sheet,  $N_{\text{bond/atom}}$  equals 1.5. Therefore, a value close to 1.5 should indicate a good interconnection between graphene flakes, thus a well-formed GA structure. However, previous studies only calculated  $N_{\text{bond/atom}}$  to illustrate that graphene flakes have been sufficiently interconnected by showing the plateau of  $N_{\text{bond/atom}}$  with increasing  $N_{\text{cycle}}$ . In this work,  $N_{\text{bond/atom}}$  is further evaluated as a function of simulation parameters, as it can serve as an important indicator of the structural properties of GAs and whether a GA can be formed by annealing cycles.  $N_{\text{bond/atom}}$  is calculated and plotted as a function of  $N_{\text{cycle}}$  under different simulation conditions (Bonds are considered to form if the distance between two carbon atoms is smaller than 1.7 Å.), as shown in Fig. 5. Fig. 5a shows the effect of  $\sigma$  (or equivalently,  $R_{\text{eff}}$ ). Error bars are calculated based on 5 different random seeds. Results show that as  $\sigma$  increases from 3.0 Å to 13.0 Å,  $N_{\text{bond/atom}}$  after 10 cycles decreases from over 1.46 to around 1.40, suggesting that a high  $\sigma$  leads to low connectivity. Nevertheless, for simulations where  $\sigma = 13.0$  Å, all 5 random seeds can still generate valid GA structures, an example provided in the SI (Fig. S7). Fig. 5b shows the effect of the inclusion-to-flake ratio  $R$  on  $N_{\text{bond/atom}}$ .  $R$  varies from 0.5 to 5.5 while other parameters are fixed. Error bars are calculated based on 5 different random seeds. Results show that as  $R$  increases from 0.5 to 5.5,  $N_{\text{bond/atom}}$  decreases from over 1.46 to around 1.42, suggesting that a high  $R$  leads to low connectivity. For simulations where  $R = 5.5$ , all 5 random seeds can still generate valid GA structures, an example provided in the SI (Fig. S8).

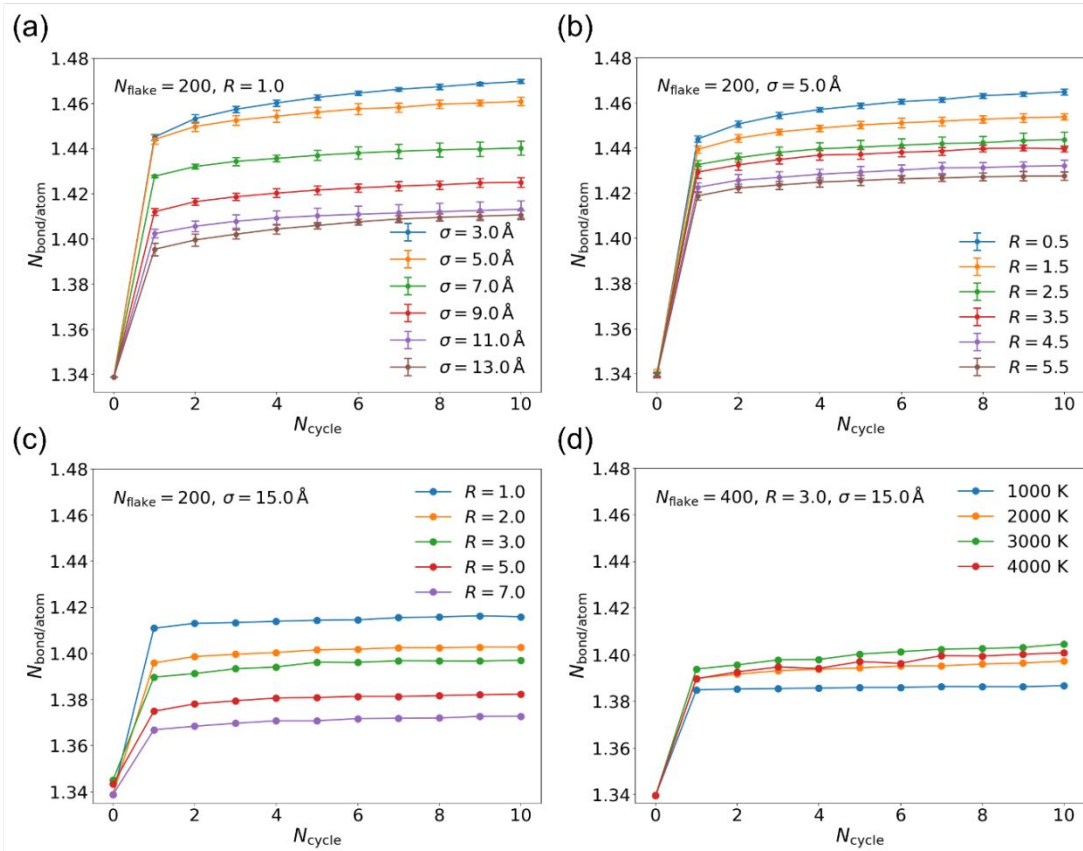


**Figure 5.** GA connectivity property in response to changes in various simulation parameters.  $N_{\text{bond/atom}}$  versus  $N_{\text{cycle}}$  plots (a) under various  $\sigma$  with  $N_{\text{flake}} = 200$  and  $R = 1.0$ , (b) under various inclusion-to-flake ratios  $R$  with  $N_{\text{flake}} = 200$  and  $\sigma = 5.0 \text{ \AA}$ , (c) under various  $R$  with  $N_{\text{flake}} = 200$  and  $\sigma = 15.0 \text{ \AA}$ , and (d) under various annealing temperature  $T_A$  with  $N_{\text{flake}} = 200$ ,  $R = 1.0$ , and  $\sigma = 5.0 \text{ \AA}$ .

However, combining a high  $\sigma$  and a high  $R$  can cause very low  $N_{\text{bond/atom}}$  values, as shown in Fig. 5c, where  $\sigma = 13.0 \text{ \AA}$  and  $R$  increases from 1.0 to 7.0.  $N_{\text{bond/atom}}$  decreases from slightly below 1.42 to around 1.37. At  $R = 2.0$  (where  $N_{\text{bond/atom}}$  after 10 cycles is about 1.40), GA structure fails to form properly where graphene flakes cannot sufficiently interconnect, as shown in the SI (Fig. S4). This structure has a density of  $146 \text{ mg}\cdot\text{cm}^{-3}$ , which is slightly higher than the lowest density previous simulation studies have studied but still about more than 10 times denser than the lightest GAs fabricated in experiments. Even though simulation techniques can be fine-tuned to achieve a lower density, this result sheds light on one of the biggest limitations of MD simulation in modeling GAs. This is because the pore size in experiments is an order of magnitude larger than the pore size in the unit cell of the MD simulations. But increasing the MD simulation scale to match the pore size in experiments is infeasible due to high computational cost.

One possible solution is increasing the number of annealing cycles  $N_{\text{cycles}}$ . In theory, the more annealing cycles the material system experiences, the higher the possibility of graphene flakes encountering each other and forming bonds. Nevertheless, it is found that only increasing  $N_{\text{cycles}}$  shows a minimal effect on  $N_{\text{bond/atom}}$ . As an example, we calculate GA structures with  $N_{\text{flake}} = 200$ ,  $R = 5.0$ ,  $\sigma = 15.0 \text{ \AA}$  and  $N_{\text{cycles}} = 10, 20, 50$ .  $N_{\text{bond/atom}}$  after these annealing cycles are 1.384, 1.386, 1.389, respectively. The GA structure after 50 annealing cycles is not properly formed, and GA structures under the three cases are provided in the SI (Fig. S5). Another solution is to increase the annealing temperature  $T_A$ . In theory, a higher temperature will lead to intensified atom movements, which will

further increase the possibility of graphene flake encounters and therefore new bond formation. The dependency of  $N_{\text{bond/atom}}$  on  $T_A$  is shown in Fig. 5d, where GAs are constructed by the following set of parameters:  $N_{\text{flake}} = 400$ ,  $R = 3.0$ ,  $\sigma = 15.0 \text{ \AA}$ ,  $N_{\text{cycles}} = 10$ , and  $T_A = 1000, 2000, 3000, 4000 \text{ K}$ . As  $T_A$  increases from 1000 K to 3000 K,  $N_{\text{bond/atom}}$  after 10 annealing cycles increases from  $\sim 1.38$  to  $\sim 1.40$ , a more significant improvement compared to increasing  $N_{\text{cycles}}$ . However,  $N_{\text{bond/atom}}$  at 4000 K is smaller than at 3000 K. This is because the high temperature has caused some of the bonds to break and GA to begin to become thermally unstable (i.e., the inability to maintain the structure integrity and functionality at an elevated temperature), thus a smaller  $N_{\text{bond/atom}}$ . An illustration of such effect is provided in the SI (Fig. S9). This temperature agrees with the melting point of graphite which ranges from 4000 to 5000 K<sup>45</sup> and that of freestanding graphene monolayers which ranges from 4000 K to 6000 K<sup>46</sup>. Therefore, the annealing temperature can be moderately increased to improve the structural integrity of GA structures.

### Effect of flake size distribution

Another opportunity to improve the connectivity of GAs is to use a different flake size distribution than the log-normal distribution, which has not been covered in the previous research. To examine whether larger graphene flakes will help improve the interconnection of graphene flakes, half-normal distributions (expressed in Eq. 4) are considered with the center set as the largest  $L$  value sampled by the log-normal distribution to bias towards larger graphene flakes. The  $\sigma_{\text{hn}}$  of the half normal distribution is a variable and  $\sigma_{\text{hn}} = 3.0 \text{ \AA}$  and  $8.0 \text{ \AA}$  are used.  $\sigma_{\text{hn}} = 3.0 \text{ \AA}$  favors larger flakes more than  $\sigma_{\text{hn}} = 8.0 \text{ \AA}$ . The probability densities of all distributions for the graphene flake size in this work are compared in Fig. 6a.

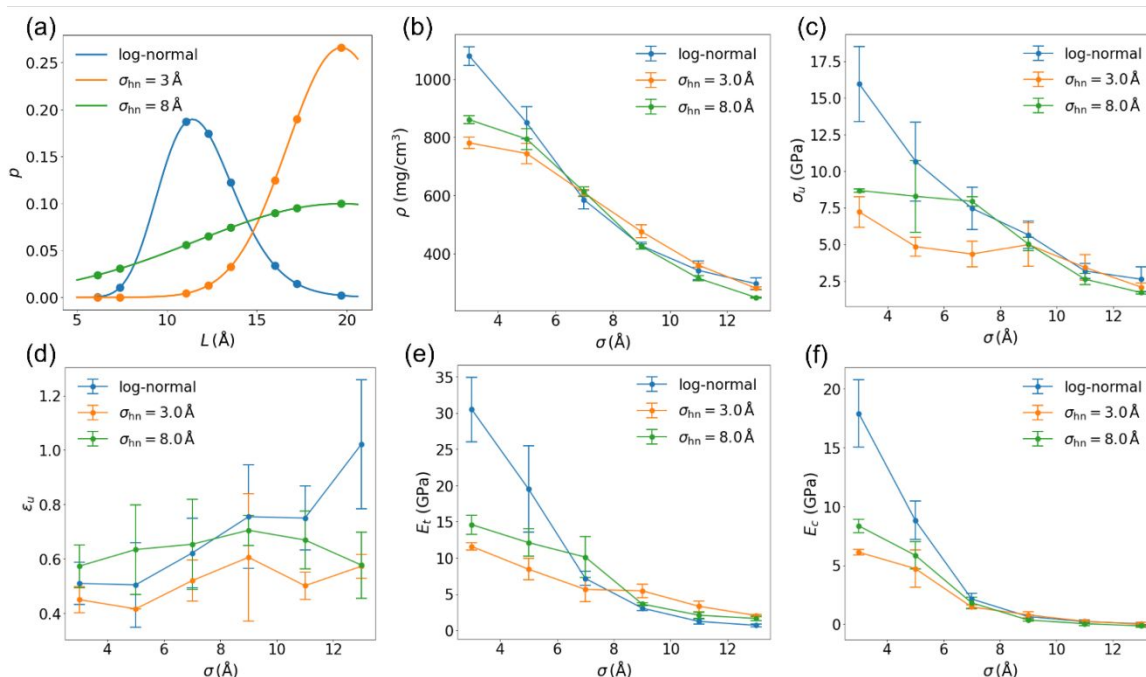


**Figure 6.** Mechanical properties of GA under different probability distributions of the graphene flake side length  $L$ . (a) Probability densities of the log-normal distribution, and half-normal distributions with  $\sigma_{\text{hn}} = 3.0 \text{ \AA}$  and  $8.0 \text{ \AA}$ . (b) Density  $\rho$ , (c) tensile strength  $\sigma_u$ , (d) tensile failure strain  $\epsilon_u$ , (e) tensile and (f) compressive moduli  $E_t$  and  $E_c$  of GA as a function of  $\sigma$  under three  $L$  distributions.

Next,  $\rho$ ,  $\sigma_u$ ,  $\epsilon_u$ ,  $E_t$ , and  $E_c$  of GAs originating from the three distributions are evaluated, as shown in Figs. 6(b-f). Results for log-normal distributions plotted here are the same as those in Fig. 2. To compare fairly,  $N_{\text{flake}} = 200$ ,  $R = 1.0$  are also used for the two half-normal distribution cases. Fig. 6b shows that for  $\sigma < \sim 6.0 \text{ \AA}$ , half-normal

distributions produce higher  $\rho$ ; for  $\sigma > \sim 6.0 \text{ \AA}$ , three distributions do not distinguish. Similar trends can be observed for tensile strength  $\sigma_u$  and moduli  $E_t$  and  $E_c$ , as shown in Figs. 6(c, e, f). However, for tensile failure strain  $\epsilon_u$ , half-normal distributions are less sensitive to  $\sigma$  compared with the log-normal distribution, as shown in Fig. 6d, suggesting that using larger graphene flakes may help reduce property randomness.

Next, the connectivity properties of GAs are studied under different flake size distributions.  $N_{\text{bond/atom}}$  as a function of  $N_{\text{cycle}}$  under  $\sigma = 5.0 \text{ \AA}$  and  $11.0 \text{ \AA}$  are shown in Fig. 7. Results show that as graphene flakes get more dominated by larger ones,  $N_{\text{bond/atom}}$  increases. This suggests that using larger graphene flakes may help improve the structural integrity of GAs. Results of  $\sigma = 3.0, 7.0, 9.0, 13.0 \text{ \AA}$  are provided in the SI (Fig. S10).

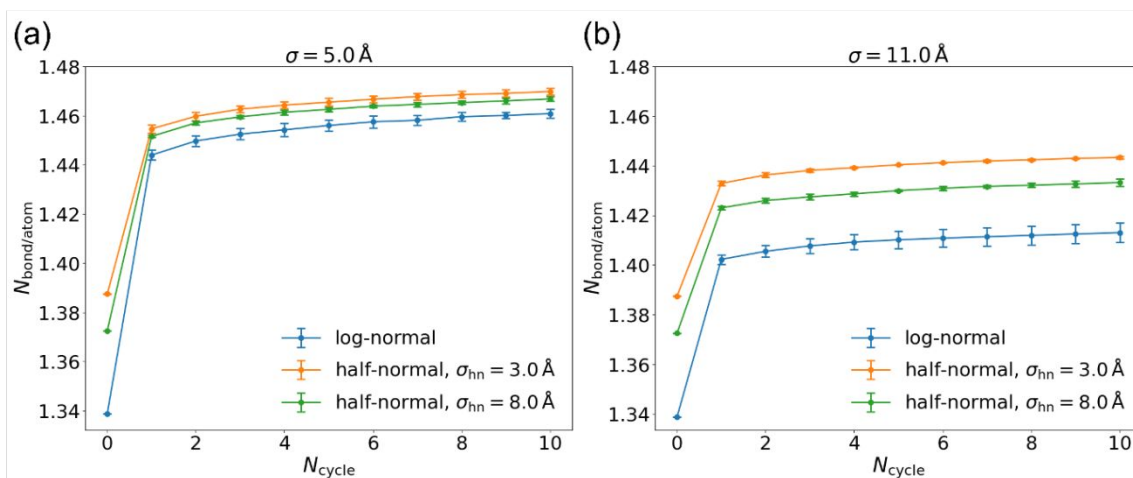


**Figure 7.** GA connectivity property under different distributions of graphene flake side length  $L$ .  $N_{\text{bond/atom}}$  versus  $N_{\text{cycle}}$  plots with (a)  $\sigma = 5.0 \text{ \AA}$  and (b)  $\sigma = 11.0 \text{ \AA}$ .

#### Comparison between simulations and experiments

Our simulation findings are compared with experimental results to showcase both the power and the limitation of the simulation modeling technique. The GAs were experimentally synthesized and characterized in our previous work<sup>47</sup>. The density of GA was tuned by loading with metal-organic framework (MOF) nanoparticles using chemical reduction method and supercritical drying. By adjusting the MOF/graphene oxide (GO) mass ratio of the precursors, MOF/GA composites of different densities were obtained. Fig. 8 shows experimental data for mechanical properties of GA including tensile strength  $\sigma_u$ , tensile failure strain  $\epsilon_u$ , tensile and compressive moduli  $E_t$  and  $E_c$  as a function of density  $\rho$ . In comparison to the simulation results in Fig. 4, the general trends for strength and moduli are similar and matching. Specifically,  $\sigma_u$ ,  $E_t$  and  $E_c$  increase as  $\rho$  increases, as shown in Figs. 8(a, c, d). However, the experimental results for strain  $\epsilon_u$  shows the opposite trends to the simulations, and the values are more than 10 times lower. This suggests that MD simulations cannot effectively capture the failure behavior of the GA, possibly due to the difference in microstructures and the defect properties. Images of GAs undergoing a catastrophic failure during tensile test are provided in the SI (Fig. S11). The comparison above between simulations and experiments indicates that MD simulations can overall capture the main trends of the mechanical properties of GA. The main limitation is that the density of the simulated GAs is much higher than our experimental GA samples, meaning that we cannot compare the values directly but only the trends. Additionally, it is worth noting that based on various synthesis recipes, the mechanical properties of synthesized GA samples vary substantially, making it very difficult to prepare ideal GA samples to compare with simulated GA structures.

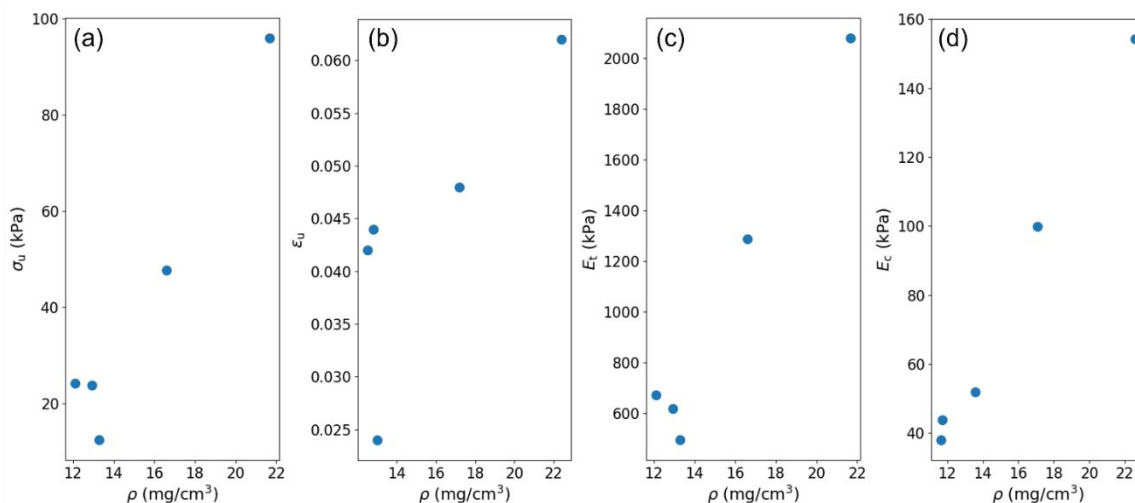


**Figure 8.** Experimental data of mechanical properties of GA as a function of density  $\rho$ . (a) tensile strength  $\sigma_u$ , (b) tensile failure strain  $\epsilon_u$ , (c) tensile and (d) compressive moduli  $E_t$  and  $E_c$  of GA as a function of  $\rho$ .

## Conclusions

In this study, to address the shortcomings of previous simulation work on GAs, we systematically study various mechanical properties and the structural integrity of GA as a function of a wide range of simulation parameters. Our contributions to the GA simulation research field are as follows. First, we cover many more parameters than previous studies. For example, the effects of both Lennard-Jones parameters  $\epsilon$  and  $\sigma$  are discussed, while previous studies only considered  $\sigma$ . Second, we additionally model the graphene size with parametrized half normal distributions on top of the previous log-normal distribution. Third, thanks to the supercomputer resources, we simulate larger material systems up to 1,500 graphene flakes in comparison with the literature<sup>22, 41-43</sup>, and illustrate the size effect on the GA properties. Lastly, we quantify the structural integrity and connectivity quality of GA structures, which has not been previously discussed in the literature. Results show that smaller and less inclusions during the *in silico* GA preparation are conducive to strength and stiffness but may lead to brittleness. It is also observed that simulating larger material systems reduces the randomness in property calculations. For the structural integrity aspect, it is shown that overly large or overly many inclusions may lead to disconnected GA structures, and that moderately increasing the annealing temperature helps alleviate this issue. Different distributions of graphene flake size are also studied, and larger flakes may improve the structural integrity and reduce the property randomness. In our simulations, the lowest density achieved is still about 10 times higher than the experimental value. We attribute this to the difference in the pore size between the simulation and the experiment, and bridging or narrowing the gap requires building larger-scale simulation models. Finally, our findings are compared with experimental results to showcase both the power and the limitation of the simulation technique. It is shown that the general trends for strength and moduli are similar while the trend for failure strain is different, possibly due to difference in microstructures and the defect properties. This work may deepen the understanding of GA simulations, accelerate materials design cycles, offer value to experimentalists in materials synthesis, and shed light on the improvement of computational approaches for GA as well as other novel nanomaterials.

## Methods

In this study, MD simulations are performed using the open-source program LAMMPS (Large-scale Atomic/Molecular Massively Parallel Simulator)<sup>48</sup>. The full atomic description is used. The total system energy is given by

$$E_{\text{total}} = E_{C-C} + E_{C-inc} + E_{inc-inc} \quad (5)$$

where  $E_{C-C}$ ,  $E_{C-inc}$ , and  $E_{inc-inc}$  denote the total energies of interactions between carbon atoms, between carbon atoms and inclusions, and between inclusions, respectively.  $E_{C-C}$  is modeled by an Adaptive Intermolecular Reactive Empirical Bond-Order (AIREBO) potential<sup>49</sup>, including short-ranged, long-ranged, and torsional terms, given by

$$E_{C-C} = E^{\text{REBO}} + E^{\text{LJ}} + E^{\text{tors}} \quad (6)$$

where  $E^{\text{REBO}}$ ,  $E^{\text{LJ}}$ , and  $E^{\text{tors}}$  are energy components corresponding to the REBO (short-ranged), Lennard-Jones (long-ranged), and torsional potentials.  $E_{C-inc}$  and  $E_{inc-inc}$  are modeled by the standard 12/6 Lennard-Jones potential, expressed as

$$E_{C-inc} = E_{inc-inc} = \sum_i \sum_{j>i} 4\epsilon \left[ \left( \frac{\sigma}{r_{ij}} \right)^{12} - \left( \frac{\sigma}{r_{ij}} \right)^6 \right] \Xi \quad (7)$$

where  $r_{ij}$  is the distance between particle  $i$  and particle  $j$ ;  $\epsilon$  is the depth of the potential well, which relates to the stiffness of the inclusion;  $\sigma$  is the distance at which the particle-particle potential energy is zero;  $\Xi$  is the cutoff function:  $\Xi = 1$  for  $r_{ij} < r_c$ , and  $\Xi = 0$  for  $r_{ij} \geq r_c$ , where  $r_c$  is the cutoff distance. In this work,  $\epsilon = 0.625 \text{ eV}^2$ ; For  $\sigma < 15.0 \text{ \AA}$ ,  $r_c = \sigma + 3.0 \text{ \AA}$  is used. For  $\sigma = 15.0 \text{ \AA}$ ,  $r_c = 21.0 \text{ \AA}$  is used. We demonstrate in the SI (Fig. S12) that larger  $r_c$  values with an increased computational cost do not significantly change the results. The mass of each spherical inclusion is set as 1 g/mol. A timestep of 1 fs is used. All carbon atoms and inclusions are initiated with a random velocity corresponding to a temperature of 300 K. The stress tensor is calculated by the following expression

$$S_{\alpha\beta} = \frac{1}{V} \left[ \sum_i \sum_{j>i} (x_{\alpha}^{(i)} - x_{\alpha}^{(j)}) \frac{\partial E_{\text{total}}}{\partial (x_{\beta}^{(i)} - x_{\beta}^{(j)})} - \sum_i m \dot{x}_{\alpha}^{(i)} \dot{x}_{\beta}^{(i)} \right] \quad (8)$$

where  $\alpha$  and  $\beta$  take on  $x$ ,  $y$  or  $z$  to generate the 6 components of the symmetric stress tensor;  $i$  and  $j$  are atom indices;  $m$  is the mass of one carbon atom;  $V$  is the volume of the simulation box.

**Conflicts of interest:** There are no conflicts of interest to declare.

**Acknowledgements:** This work used the Extreme Science and Engineering Discovery Environment (XSEDE) Bridges system, which is supported by National Science Foundation (Fund number ACI-1548562). The authors acknowledge support from the Alfred P. Sloan Foundation and the National Science Foundation (Fund Number: DMREF-2119276, 1929363, and 1929447).

## References

1. C. Berger, Z. Song, T. Li, X. Li, A. Y. Ogbazghi, R. Feng, Z. Dai, A. N. Marchenkov, E. H. Conrad, P. N. First and W. A. de Heer, *J. Phys. Chem. B*, 2004, **108**, 19912-19916.
2. F. Withers, M. Dubois and A. K. Savchenko, *Phys. Rev. B*, 2010, **82**, 073403.
3. D. G. Sangiovanni, R. Faccio, G. K. Gueorguiev and A. Kakanakova-Georgieva, *Phys. Chem. Chem. Phys.*, 2023, **25**, 829-837.
4. A. A. Balandin, S. Ghosh, W. Bao, I. Calizo, D. Teweldebrhan, F. Miao and C. N. Lau, *Nano Lett.*, 2008, **8**, 902-907.
5. A. A. Balandin, *Nat. Mater.*, 2011, **10**, 569-581.
6. C. Lundgren, A. Kakanakova-Georgieva and G. K. Gueorguiev, *Nanotechnol.*, 2022, **33**, 335706.

7. P. Zhang, L. Ma, F. Fan, Z. Zeng, C. Peng, P. E. Loya, Z. Liu, Y. Gong, J. Zhang, X. Zhang, P. M. Ajayan, T. Zhu and J. Lou, *Nat. Commun.*, 2014, **5**, 3782.
8. B. Zheng and G. X. Gu, *Carbon*, 2019, **155**, 697-705.
9. C. Lee, X. Wei, J. W. Kysar and J. Hone, *Science*, 2008, **321**, 385-388.
10. B. Zheng, Z. Zheng and G. X. Gu, *npj Computational Materials*, 2022, **8**, 225.
11. J. Sha, Y. Li, R. Villegas Salvatierra, T. Wang, P. Dong, Y. Ji, S.-K. Lee, C. Zhang, J. Zhang, R. H. Smith, P. M. Ajayan, J. Lou, N. Zhao and J. M. Tour, *ACS Nano*, 2017, **11**, 6860-6867.
12. A. Idowu, B. Boesl and A. Agarwal, *Carbon*, 2018, **135**, 52-71.
13. E. Singh, Z. Chen, F. Houshmand, W. Ren, Y. Peles, H.-M. Cheng and N. Koratkar, *Small*, 2013, **9**, 75-80.
14. G. Gorgolis and C. Galiotis, *2D Mater.*, 2017, **4**, 032001.
15. M. A. Worsley, P. J. Pauzauskie, T. Y. Olson, J. Biener, J. H. Satcher, Jr. and T. F. Baumann, *J. Am. Chem. Soc.*, 2010, **132**, 14067-14069.
16. H. Hu, Z. Zhao, W. Wan, Y. Gogotsi and J. Qiu, *Adv. Mater.*, 2013, **25**, 2219-2223.
17. X. Cao, Y. Shi, W. Shi, G. Lu, X. Huang, Q. Yan, Q. Zhang and H. Zhang, *Small*, 2011, **7**, 3163-3168.
18. Y. Ma and Y. Chen, *Natl. Sci. Rev.*, 2014, **2**, 40-53.
19. J. Qin, C. He, N. Zhao, Z. Wang, C. Shi, E.-Z. Liu and J. Li, *ACS Nano*, 2014, **8**, 1728-1738.
20. Z. Chen, W. Ren, L. Gao, B. Liu, S. Pei and H.-M. Cheng, *Nat. Mater.*, 2011, **10**, 424-428.
21. H. Sun, Z. Xu and C. Gao, *Adv. Mater.*, 2013, **25**, 2554-2560.
22. Z. Qin, G. S. Jung, M. J. Kang and M. J. Buehler, *Sci. Adv.*, 2017, **3**, e1601536.
23. J.-Y. Hong, E.-H. Sohn, S. Park and H. S. Park, *Chem. Eng. J.*, 2015, **269**, 229-235.
24. T. Liu, M. Huang, X. Li, C. Wang, C.-X. Gui and Z.-Z. Yu, *Carbon*, 2016, **100**, 456-464.
25. H. Hu, Z. Zhao, Y. Gogotsi and J. Qiu, *Environ. Sci. Technol. Lett.*, 2014, **1**, 214-220.
26. A. Harley-Trochimczyk, J. Chang, Q. Zhou, J. Dong, T. Pham, M. A. Worsley, R. Maboudian, A. Zettl and W. Mickelson, *Sens. Actuators B: Chem.*, 2015, **206**, 399-406.
27. Y. Zhao, X. Xie, J. Zhang, H. Liu, H.-J. Ahn, K. Sun and G. Wang, *Chem. Eur. J.*, 2015, **21**, 15908-15913.
28. H. Yin, C. Zhang, F. Liu and Y. Hou, *Adv. Funct. Mater.*, 2014, **24**, 2930-2937.
29. R. Wang, K.-Q. Lu, F. Zhang, Z.-R. Tang and Y.-J. Xu, *Appl. Catal., B*, 2018, **233**, 11-18.
30. Z. Xu, Y. Zhang, P. Li and C. Gao, *ACS Nano*, 2012, **6**, 7103-7113.
31. C. Zhu, T. Y.-J. Han, E. B. Duoss, A. M. Golobic, J. D. Kuntz, C. M. Spadaccini and M. A. Worsley, *Nat. Commun.*, 2015, **6**, 6962.
32. Z. Yu, M. McInnis, J. Calderon, S. Seal, L. Zhai and J. Thomas, *Nano Energy*, 2015, **11**, 611-620.
33. R. Liu, L. Wan, S. Liu, L. Pan, D. Wu and D. Zhao, *Adv. Funct. Mater.*, 2015, **25**, 526-533.
34. Y. Yang, Y. Xi, J. Li, G. Wei, N. I. Klyui and W. Han, *Nanoscale Res. Lett.*, 2017, **12**, 394.
35. X. Liu, J. Cui, J. Sun and X. Zhang, *RSC Adv.*, 2014, **4**, 22601-22605.
36. H. Long, A. Harley-Trochimczyk, T. Pham, Z. Tang, T. Shi, A. Zettl, C. Carraro, M. A. Worsley and R. Maboudian, *Adv. Funct. Mater.*, 2016, **26**, 5158-5165.
37. J. Xie, L. Niu, Y. Qiao, P. Chen and D. Rittel, *Mater. Des.*, 2022, **221**, 110912.
38. L. Niu, J. Xie, P. Chen, G. Li and X. Zhang, *Diam. Relat. Mater.*, 2021, **111**, 108225.
39. Y. Cheng, S. Zhou, P. Hu, G. Zhao, Y. Li, X. Zhang and W. Han, *Sci. Rep.*, 2017, **7**, 1439.
40. Q. Zhang, X. Xu, H. Li, G. Xiong, H. Hu and T. S. Fisher, *Carbon*, 2015, **93**, 659-670.
41. S. P. Patil, P. Shendye and B. Markert, *J. Phys. Chem. B*, 2020, **124**, 6132-6139.
42. S. P. Patil, A. Kulkarni and B. Markert, *Comput. Mater. Sci.*, 2021, **189**, 110252.
43. B. Zheng, Z. Zheng and G. X. Gu, *Nano Futures*, 2021, **5**, 045004.
44. X. Xie, Y. Zhou, H. Bi, K. Yin, S. Wan and L. Sun, *Sci. Rep.*, 2013, **3**, 2117.
45. A. I. Savvatimskiy, *Carbon*, 2005, **43**, 1115-1142.
46. E. Ganz, A. B. Ganz, L.-M. Yang and M. Dornfeld, *Phys. Chem. Chem. Phys.*, 2017, **19**, 3756-3762.
47. Z. Li, C. Liu, J. J. Frick, A. K. Davey, M. N. Dods, C. Carraro, D. G. Senesky and R. Maboudian, *Carbon*, 2023, **201**, 561-567.

48. A. P. Thompson, H. M. Aktulga, R. Berger, D. S. Bolintineanu, W. M. Brown, P. S. Crozier, P. J. in 't Veld, A. Kohlmeyer, S. G. Moore, T. D. Nguyen, R. Shan, M. J. Stevens, J. Tranchida, C. Trott and S. J. Plimpton, *Comp. Phys. Commun.*, 2022, **271**, 108171.
49. S. J. Stuart, A. B. Tutein and J. A. Harrison, *J. Chem. Phys.*, 2000, **112**, 6472-6486.